Supplementary information

Arthur Ishteev[a], Kamilla Konstantinova[a], Georgy Ermolaev[b], Dmitry Kiselev[c], Dmitry S. Muratov[a], Marina Voronova[c], Tatyana Ilina[c], Peter Lagov[a], Oleg Uvarov[e], Yuri Pavlov[d], Marta Letovaltseva[f], Aleksey Arsenin[b], Valentyn Volkov[b], Sergey Didenko[a], Danila Saranin[a], Aldo Di Carlo[a,g]

[a]LASE - Laboratory of Advanced Solar Energy, NUST MISiS, 119049 Moscow, Russia

[b]Center for Photonics and 2D Materials, Moscow Institute of Physics and Technology,

Dolgoprudny 141700, Russia

[c]Laboratory of Physics of Oxide Ferroelectrics NUST MISiS, 119049 Moscow, Russia

[d]A.N. Frumkin Institute of Physical Chemistry and Electrochemistry Russian Academy of Sciences (IPCE RAS), 119071, Moscow, Russia

[e]Prokhorov General Physics Institute of the Russian Academy of Sciences, 119991, Moscow, Russia

[f]Russian Technological University MIREA (RTU MIREA), Moscow, Russia

[g]CHOSE - Centre of Hybrid and Organic Solar Energy, Department of Electronics Engineering, Rome, Italy

Corresponding Authors: arturishteev@misis.ru, aldo.dicarlo@uniroma2.it

Experimental

Materials

The following materials were used for the growth of $MAPbBr_3$ MNCs without any purification treatments after purchase:

Methylammonium Bromide (MABr; 99.99 % CAS #6876-37-5); lead (II) bromide ($PbBr_2$, ultra-dry, 99.999% 10 mesh beads CAS #10031-22-8); N,N-Dimethylformamide (DMF, 99.8%, extra dry, AcroSeal, Thermo Scientific, CAS #68-12-2); dimethyldimethoxysilane (CAS № 1112-39-6); isopropanol (99.5%, extra dry, Thermo Scientific CAS #67-63-0).

The growth of single-crystal $CH_3NH_3Br_3$ by solvent surface engineering and space-confined growth

Perovskite monocrystals were synthesized from solution 1:1 mmol CH_3NH_3Br:$PbBr_2$ precursors ratio. 224 mg of CH_3NH_3Br and 734 mg of $PbBr_2$ were dissolved in 2 ml of dimethylformamide (DMF). The solution was prepared under argon atmosphere and had been stirred overnight at room temperature. The solution was filtered three times through PTFE 0.45μm syringe filters before the growth process.

Hydrophobic treatment of the substrate has been employed to reduce the number of nucleation centers. Vials were treated with dimethyldimethoxysilane to decrease the wetting angle between the glass surface and DMF.

A small seed crystal (typically less than 1 mm^3) was dipped into the solution. The solution temperature was increased at a rate 8° per hour in the range from 68 to 78°C. Then the rate was decreased till 8° per hour to 90°C.

At the end of the process, on the bottom of the vial, the $CH_3NH_3Br_3$ single-crystal cubic shape reaches 6×6×3 mm in size.

Several routes of $MAPbBr_3$ crystal synthesis have been considered to optimize the size and quality of the crystal as reported in table S1. At the very beginning, we tried to reproduce literature approaches[1,2,3] by using inverse temperature crystallization. First results showed spontaneous nucleation of sugar grain size 1x1mm over a dozen in each volume of equimolar solution (fig. S1a). At the same time, we tested different ratios suggested in the literature [4] with excess of MABr to $PbBr_2$ component ratios. Unfortunately, we did not obtain measurable samples and we re-considered optimization of equimolar solution only. In the optimization phase, we found that filtration of the solution prior to growth process helps to decrease a number of nucleated crystals that compete with each other during the growth period (fig. S1b). Then, hydrophobic treatment of the synthesis volume (glass vial) [5] decreased further the number of nucleation sites till to one single crystal in the entire volume (fig. S1c). Moreover, we decreased the rate of temperature growth and insulate the crystal farm from vibration by setting it on top of marble table with resin pads (fig. S1d). Overall, we got a very reproducible recipe to get samples up to 6x6mm with very clear optical media (no defects) as shown in fig. S1d. It was appropriate size for XRD and optics measurements.

Table S1: selected lines from MAPbBr3 monocrystals database.

Name	Date	m(MABr), mg	m(PbBr), mg	Volume, ml	Filtration	T1 °C	T2°C	T3 °C	ΔT1-2 °C	ΔT2-3°C	Quantity	Max, mm
MBr 01	12.05.2021	224	734	2	-	68	79	90	2	1	>10	1x1
MBr 02	17.05.2021	224	734	2	-	68	78	90	2	1	>15	1x1
MBr 05	21.05.2021	123,2	367	2	-	68	-	100	3	2	-	-
MBr 06	21.05.2021	112	403,7	2	-	68	-	100	3	2	-	-
MBr II 02	24.05.2021	1120,06	3670	2	yes	72	78	90	3	2	>5	4x4 cube
MBr II 03	24.05.2021	1120,06	3670	2	yes	68	78	90	3	2	>5	3x3 plate
C4	26.06.2021	896	2936	2	yes x2	68	78	90	2	1	1	5x5

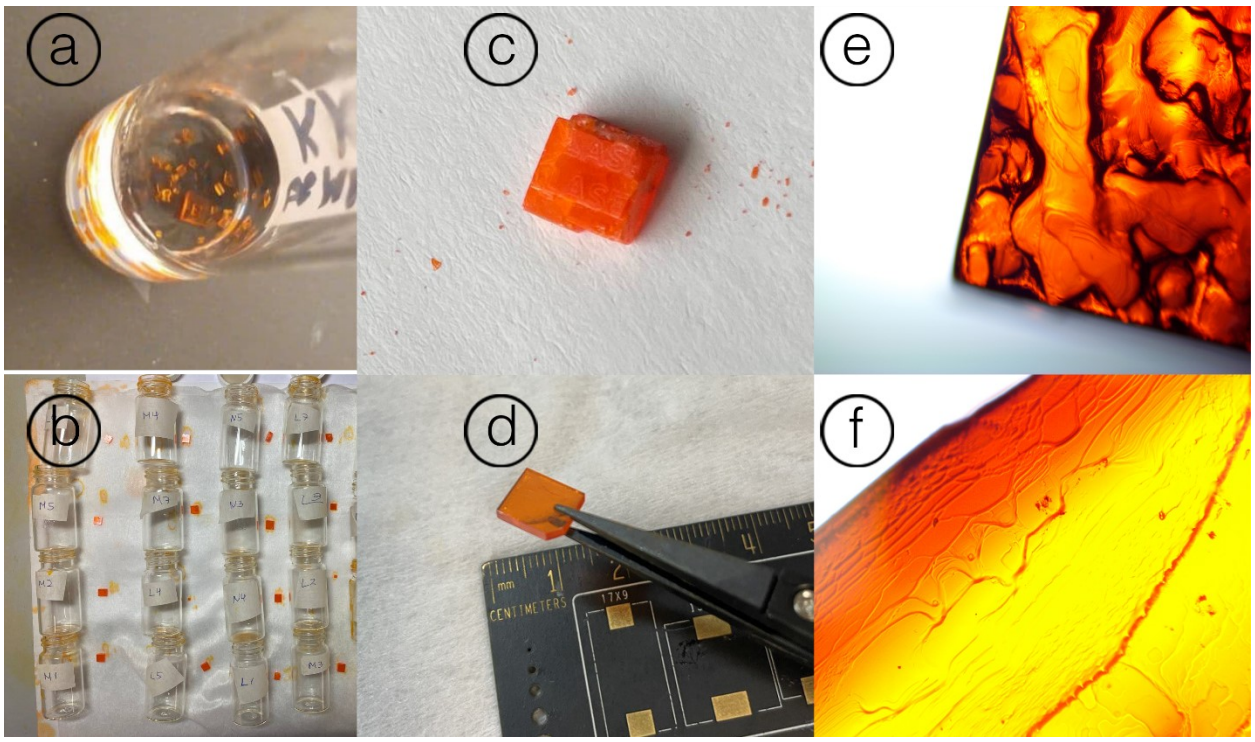

Figure S1 — a) sugar grain size crystals; b) crystal farm harvesting; c) photo of the crystal grown under vibration and high temperature rate; d) image of the large clean crystal after synthesis; e) optical microscopy imaging of natural surface of monocrystal under high heating rate; f) optical microscopy imaging of natural surface of monocrystal under low heating rate.

Mechanical preparation was divided into two operations: grinding and polishing. Initially, the surface was formed by grinding with a fixed abrasive. We used a diamond surface grinding wheel with a roughness of 14-20 microns. Dry Isopropyl alcohol (IPA) was used as a lubricant. After the formation of the plane, polishing was performed. Polishing was carried out on a Struers LaboSystem installation. We used Synthetic short nap Polishing Cloths (Struers MD-Nap), with 0.8 micron cerium oxide optical polishing powder. Dry isopropyl alcohol was also used as a lubricant. The roughness of the resulting surface was measured at 5 different points on the surface using a Scanning Probe Microscope MFP 3D Stand Alone (Asylum Research). The average roughness value was R_a= 42 nm.

Irradiation of samples under fast electron flux

Electron irradiation was performed in a linear electron accelerator, with electron energy 5 MeV, electron flux $(3\pm1)\cdot10^{12}$ $cm^{-2}\cdot s^{-1}$, with fluencies 10^{15} electrons/cm^{-2}. The electron beam current and fluence were monitored using a Faraday cup (film polymer dosimeters based on a copolymer with phenazine dye). Irradiation was carried out through the sample and plastic container in the air atmosphere.

Investigation of structural properties for $MAPbBr_3$ MNCs

XRD patterns were recorded on Brucker D8 Discover X-ray diffractometer with Cu Kα radiation (1.54184 Å).

Investigation of optical properties for $MAPbBr_3$ MNCs

Spectroscopic ellipsometry

Spectroscopic ellipsometry (SE) measurements were performed on a variable-angle spectroscopic ellipsometer (VASE, J.A. Woollam Co.) over a wide wavelength range from 300 to 3300 nm in steps of 1 nm. SE data were taken at multiple angles of incidence from 50° to 70° in steps of 5°. The optical properties were analytically acquisited from ellipsometry amplitude component ψ and the phase difference Δ. Generally, the equation (1) determines pseudo-dielectric function. The pseudo-dielectric function does not depend on the incident angles of the measurements. Since the different incident angles give the same result for a pseudo-dielectric function, that means it is the dielectric function.

Optical constants were obtained from the analytical formula at the assumption of reflection at single interface air-perovskite[6]:

$$\tilde{n} = \sqrt{\tilde{\varepsilon}} = \sqrt{\sin^2(\theta)\left(1 + \tan^2(\theta)\left(\frac{1-\rho}{1+\rho}\right)^2\right)} \qquad (1)$$

where ρ is the complex reflectance ratio, measured by ellipsometer, θ is the incident angle, $\tilde{n}$ and $\tilde{\varepsilon}$ are complex refractive index and dielectric permittivity, respectively.

Photoluminescence measurements

Luminescent properties and crystal defects were characterized by two photons excitation confocal microscopy (2PEF). The investigation was carried out on Carl Zeiss LSM 710 NLO microscopy. The excitation wavelength of 800 nm was applied by a laser at 80 MHz and a pulse width of 150 femtoseconds. The laser power was set on 0.1 W. Photoluminescence spectra were recorded in the range 440-725 nm with 10nm resolution. The 2PEF method allows us to measure PL spectra in depth.

Investigation of surface electrical properties for $MAPbBr_3$ MNCs

Kelvin probe force microscopy (KPFM) or Kelvin mode mappings were carried out with an MFP-3D (Asylum Research, Oxford Instruments, Santa Barbara, USA) commercial scanning probe using a NSG30/Pt (Tipsnano, Tallinn, Estonia) conductive probe with a spring constant of 37 N/m.

For KPFM measurements, the probe scans the surface topography using tapping mode first and then a 1 V AC voltage was applied on the probe near its resonance frequency (~272 kHz) to measure the sample surface potential distribution through a DC voltage feedback loop. The scan rate was set to 0.6 Hz, scan size 15×15μm^2 with resolution 512×512 pixels, and a lift scan height of approximately 50 nm was adopted. The same probe was used to study the samples before and after irradiation. The work function of the conductive tips (~4.77 eV) was calibrated with freshly cleaved highly oriented pyrolytic graphite (HOPG, Asylum Research, Oxford Instruments, Santa Barbara, USA, ~4.65 eV).

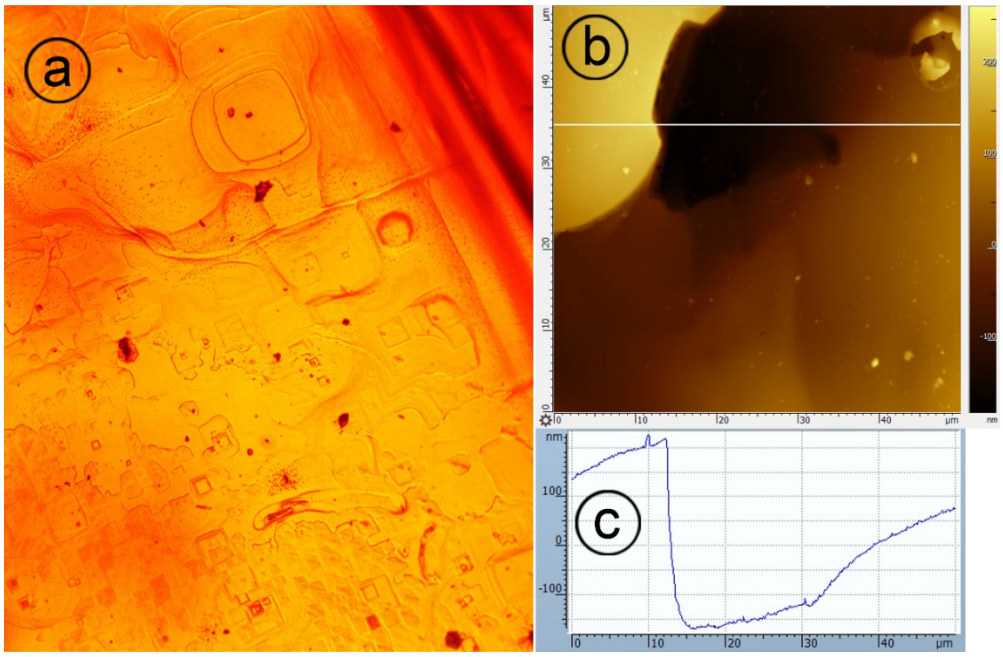

Figure S2 – as-grown $MAPbBr_3$ MNC surface: a) optical microscopy (x5) imaging; b) atomic force microscopy imaging; c) roughness profiling

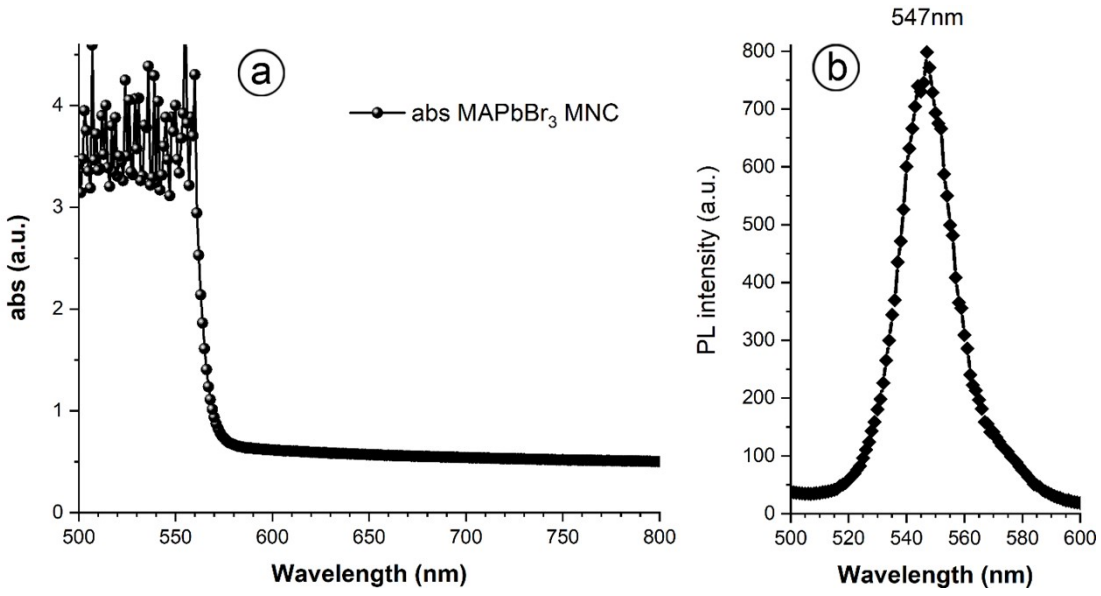

Figure S3 – $MAPbBr_3$ MNC spectrums: a) absorption spectrum measured with UV-VIS transmission b) photoluminescence measured with UV-excitation

Although we used high electron energy and the high dose in the experiment, we did not find clear evidence of formation of metallic lead after irradiation at least in our detection range (2%). We analyzed XRD pattern of pristine and irradiated crystals in logarithmical scale (figure S4). Compared to pristine crystal, there are extra tiny peaks after irradiation. There are reflections at 28.95° and 43.77° points to Cu-K_W; 27.16° and 41.24° points to Cu-K_β lines. These lines are the same for pristine and irradiated samples. The lines at 21.77°, 23.79°, 33.75° and 37.13° are tiny signals of $PbBr_2$ [9] on the surface mainly induced by the sample heating under electron flow irradiation. Metalic lead lines do not match to any peaks on the XRD pattern.

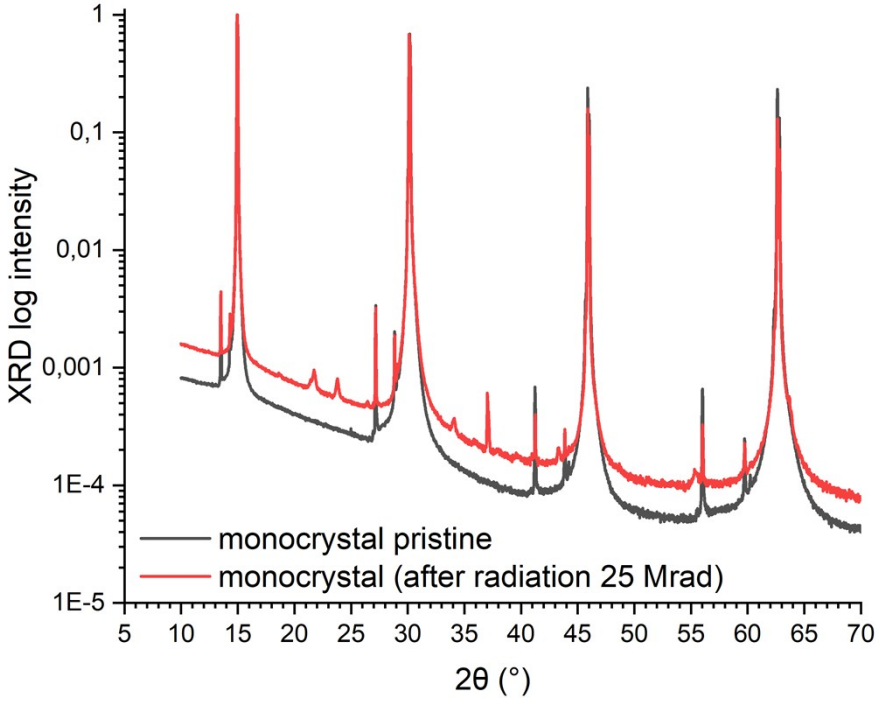

Figure S4 - XRD patterns of $CH_3NH_3PbBr_3$ before radiation (black line), and after radiation (25Mrad) (red line) at logarithmic scale

In the event of the lead formation after irradiation, we would also observe metallic response in the infrared spectral range. Indeed, in that case, optical constants would follow effective medium approximation with the effective complex refractive[10] index $\tilde{n}_{eff} = \tilde{n}_{Pb} \cdot p + \tilde{n}_{perovskite} \cdot (1 - p)$, where $\tilde{n}_{Pb}$ and $\tilde{n}_{perovskite}$ are complex refractive indices of lead and perovskite, respectively, and p is the lead concentration. For example, even 2% of lead would result for mid-infrared wavelengths ($\lambda \sim 3$ μm) in effective extinction[11] coefficient $k = Im[\tilde{n}_{eff}] \approx k_{Pb} \cdot p \approx 16 \cdot 0.02 = 0.32$. Meanwhile,

ellipsometry measurements (Figure 2a) show extinction coefficient to be less than 0.2, which means that the lead concentration is less than 2%.

We cannot exclude however the formation of metallic lead as reported by other investigations at much lower doses of radiation[12,13]. Nevertheless, it is very remarkable that increasing the electron energy by a factor 100 (as well the dose) with respect to literature, we do not find a detectable signal of metallic lead

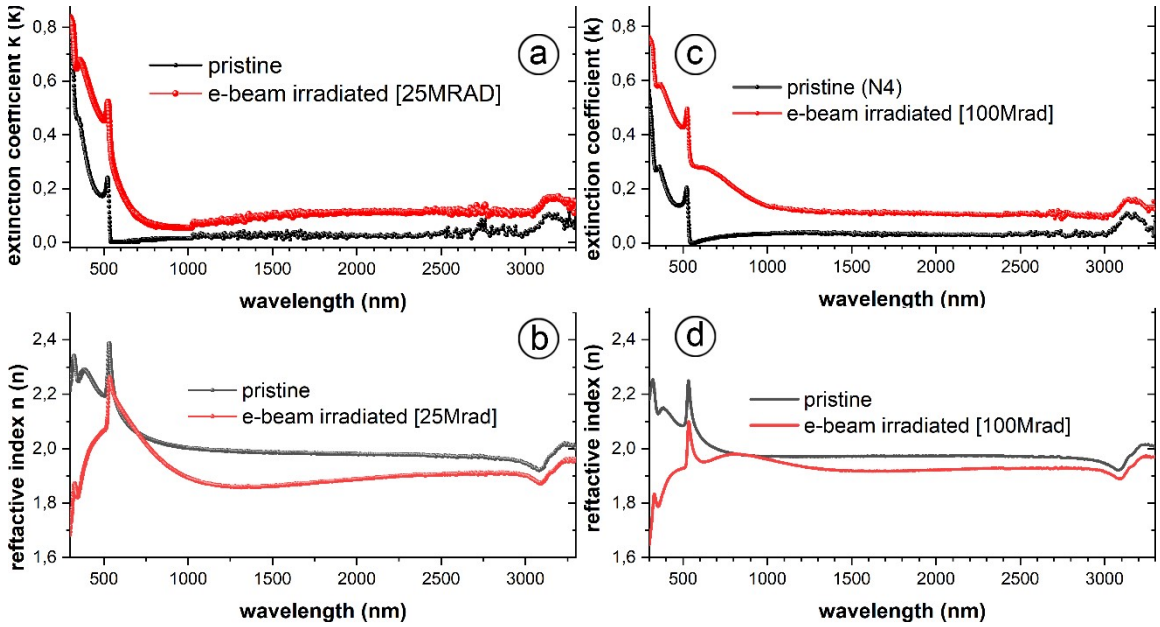

Figure S5 – $MAPbBr_3$ MNC extinction coefficient and refractive index in range 300-3300nm for crystals stressed under e-beam irradiation 25Mrad: a) and b); 100Mrad c) and d) respectively

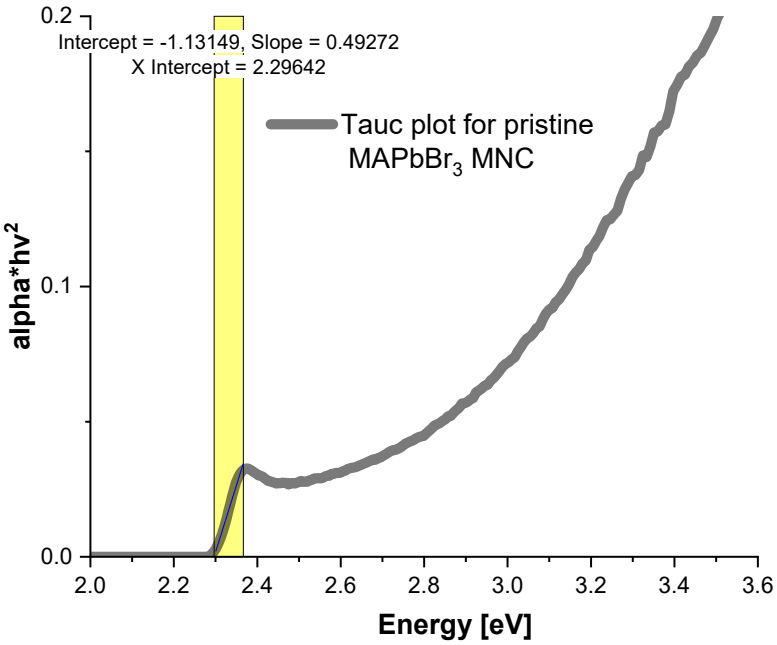

Figure S6 – Tauc plot for pristine $MAPbBr_3$ MNC with linear fitting for the determination of the band gap value with the edge of absorption

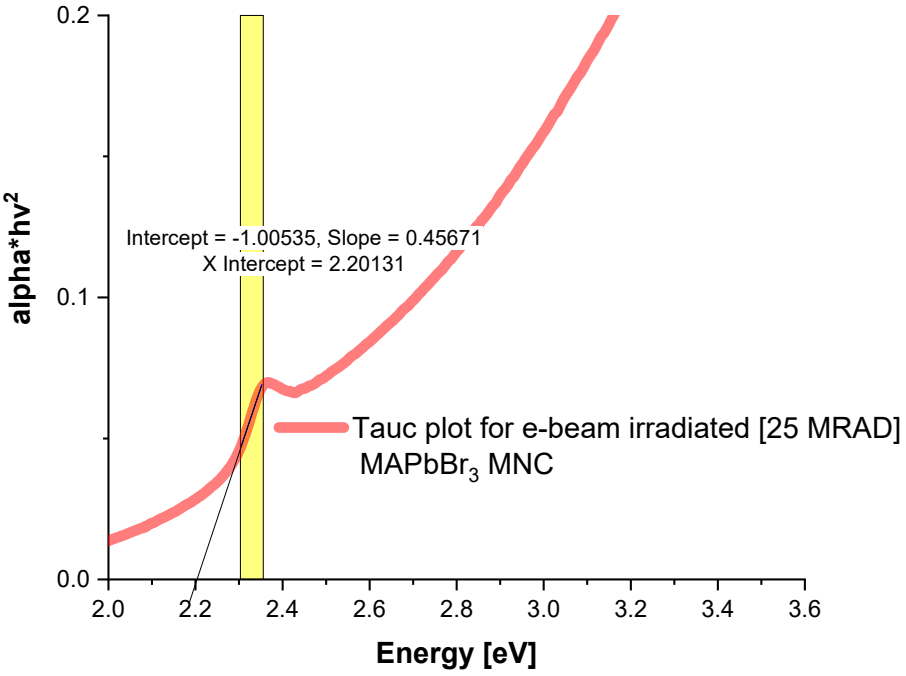

Figure S7 - Tauc plot for e-beam irradiated [25 MRAD] $MAPbBr_3$ MNC with linear fitting for the determination of the band gap value with the edge of absorption

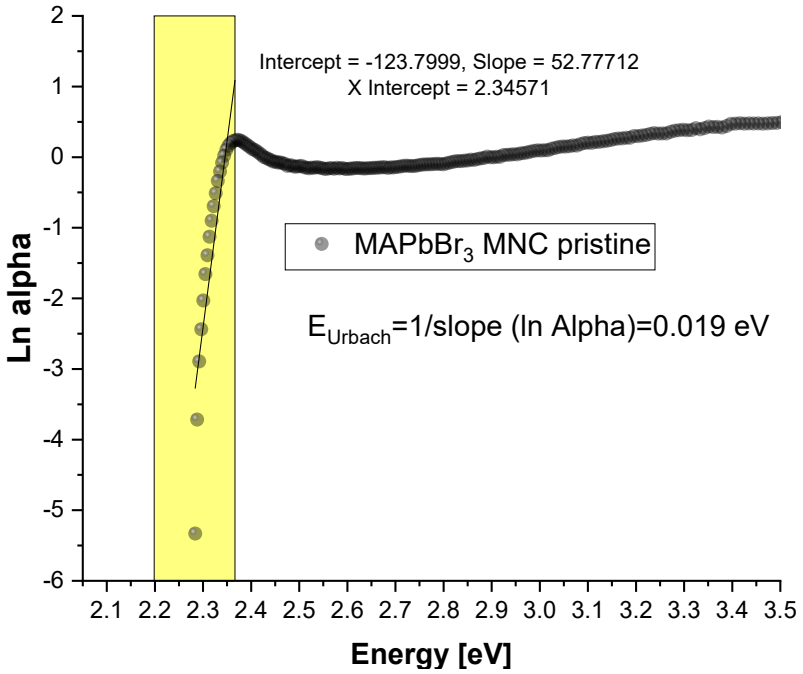

Figure S8 – The extraction of the Urbach energy values from the logarithmic plot of the absorption coefficient for pristine $MAPbBr_3$ MNC

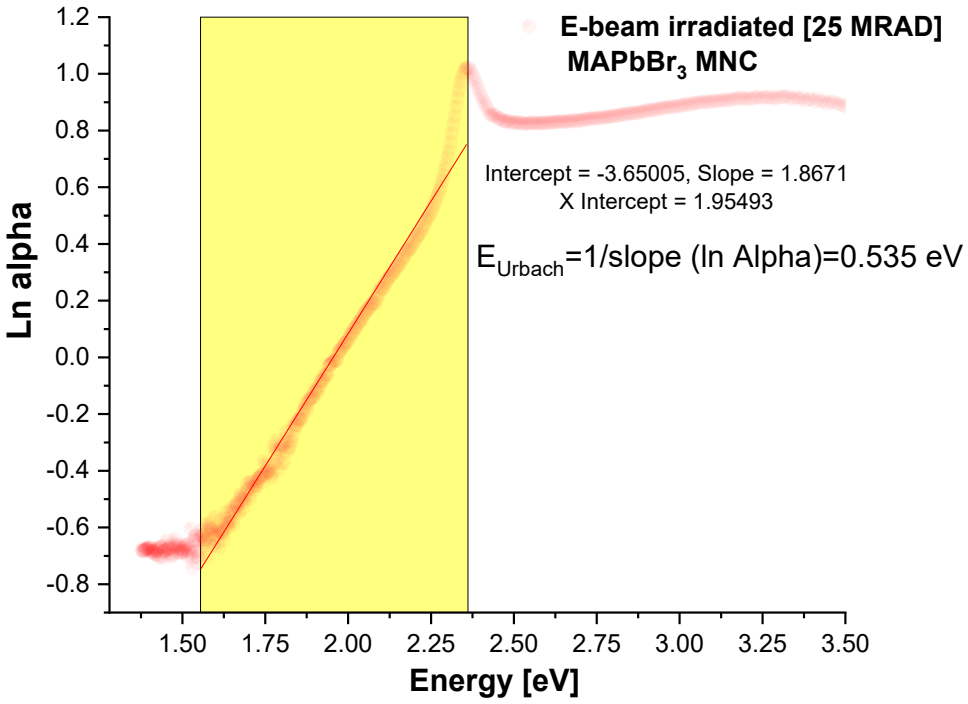

Figure S9 – The extraction of the Urbach energy values from the logarithmic plot of the absorption coefficient for e-beam -irradiated $MAPbBr_3$ MNC

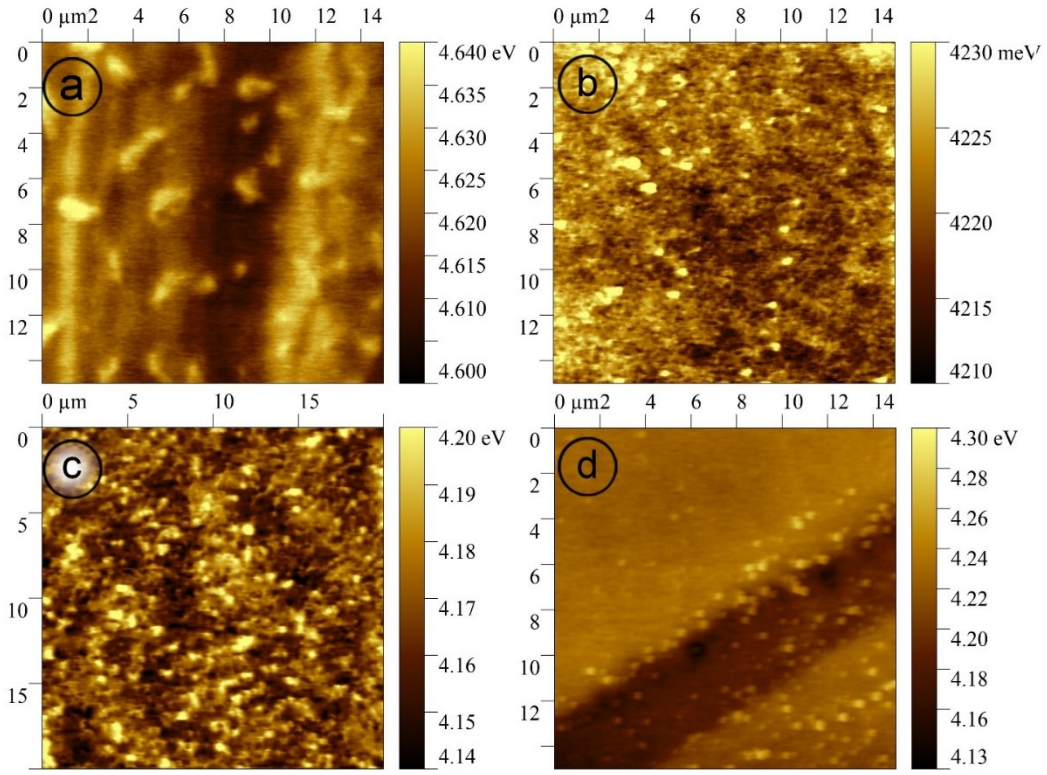

Figure S10 – KPFM imaging of work function imaging on a) pristine crystal, b) the same irradiated (25Mrad) crystal spot 1, c) the same irradiated crystal another spot, d) the same irradiated crystal another spot 2

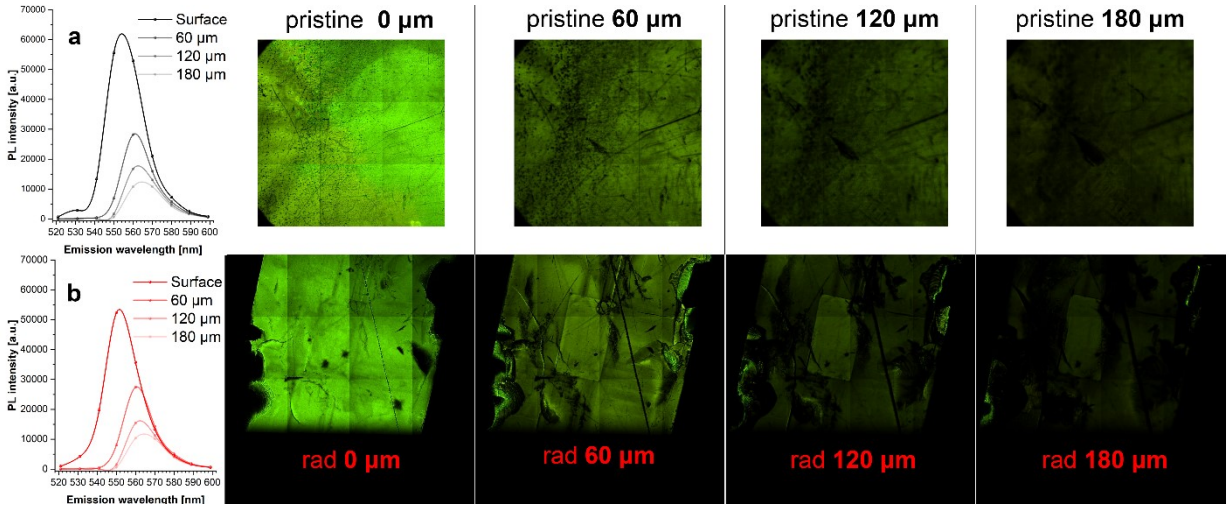

Figure S11 – photoluminescence mapping of irradiated 25Mrad (top line) and pristine (bottom line) captured by 2PEF method from a) surface and depth b)60 µm, c) 120 µm, d) 180 µm

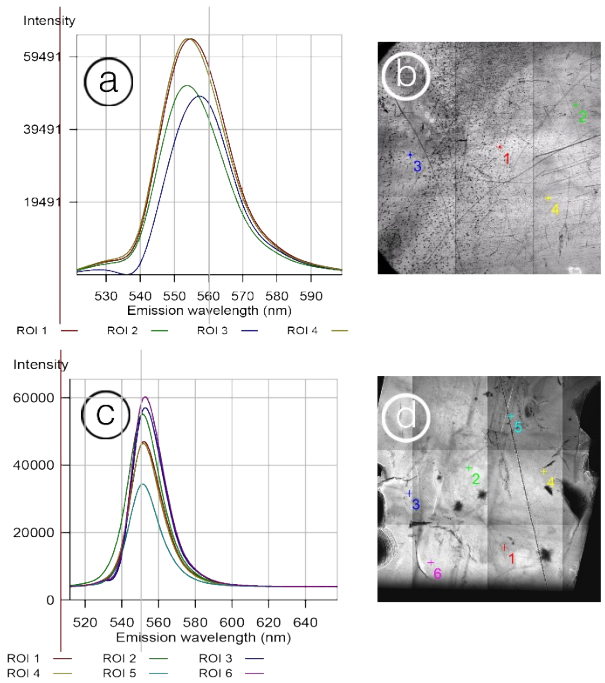

Figure S12 – a) PL signals arising from several points of the surface of pristine crystal. b) pristine crystal surface maps with the indication of sampling points for the PL reported in a). c) PL signals arising from several points of the surface of irradiated crystal. d) irradiated crystal surface maps with the indication of sampling points for the PL reported in c).

We observe small fluctuation of the PL peak position varying the acquisition point on the surface of the crystal as shown in fig. S12. Among the measured points we observe a fluctuation of the peak position of 5nm (fig. S11a and b) which is also similar for the PL peak of irradiated surface (fig. S12c and d). This fluctuation is most probably related to the two photons excitation confocal microscopy we used to measure the PL. Some of the peaks (see ROI3 of Fig. S12a, for example) present a clear sign of reabsorption showing that the signal is coming slightly below the surface. Such reabsorption can cause the observed peak shift.

References

1 Z. Fan, J. Liu, W. Zuo, G. Liu, X. He, K. Luo, Q. Ye and C. Liao, *Phys. Status Solidi Appl. Mater. Sci.*, 2020, **217**, 1–8.

2 M. I. Saidaminov, A. L. Abdelhady, G. Maculan and O. M. Bakr, *Chem. Commun.*, 2015, **51**, 17658–17661.

3 M. I. Saidaminov, A. L. Abdelhady, B. Murali, E. Alarousu, V. M. Burlakov, W. Peng, I. Dursun, L. Wang, Y. He, G. MacUlan, A. Goriely, T. Wu, O. F. Mohammed and O. M. Bakr, *Nat. Commun.*, 2015, **6**, 1–6.

4 G. A. Ermolaev, A. P. Tsapenko, V. S. Volkov, A. S. Anisimov, Y. G. Gladush and A. G. Nasibulin, *Appl. Phys. Lett.*, 2020, **116**, 1–5.

5 Y. H. Deng, Z. Q. Yang and R. M. Ma, *Nano Converg.*, , DOI:10.1186/s40580-020-00236-5.

6 G. A. Ermolaev, A. P. Tsapenko, V. S. Volkov, A. S. Anisimov, Y. G. Gladush and A. G. Nasibulin, *Appl. Phys. Lett.*, 2020, **116**, 1–5.

7 G. A. Ermolaev, S. E. Kushnir, N. A. Sapoletova and K. S. Napolskii, *Nanomaterials*, 2019, **9**, 1–12.

8 A. I. Golovashkin, I. E. Leksina, G. P. Motulevich and A. A. Shubin, *Sov. Phys. JETP*, 1968, **26**, 881–887.

9 W. Nieuwenkamp and J. M. Bijvoet, Zeitschrift fuer Krist. Krist. Krist. Krist., 1932, 84, 49–61.

10 G. Divitini, S. Cacovich, F. Matteocci, L. Cinà, A. Di Carlo and C. Ducati, Nat. Energy, , DOI:10.1038/NENERGY.2015.12.

11 H. Syafutra, J. H. Yun, Y. Yoshie, M. Lyu, S. N. Takeda, M. Nakamura, L. Wang and M. C. Jung, Nanomaterials, 2020, 10, 1–8.